$LiNbO_3$-Based Synaptic Sensors via Microring Resonator Modulators

Ceren Babayigit, Rahim Esfandyarpour, and Ozdal Boyraz

***Abstract*—The precise measurement of action potentials with high sensitivity and broad bandwidth (BW) is crucial in neuroscience research. However, current electrode-based methods are limited by BW, sensitivity to biological noise, and tissue damage caused by measurement byproducts. To address these challenges, we propose a novel optrode that leverages the electrooptic (EO) effect of lithium niobate to detect electric fields generated by voltage differences in the extracellular medium. This new approach combines the EO effect with a ring resonator and coherent balance detector, enabling highly sensitive and precise action potential measurements. We demonstrate the feasibility of this optrode by carrying the signal with modulation and beating it through coherent detection to detect weak signals. The array configuration of the sensor offers multiplexed sensing capabilities, enabling simultaneous detection of neural activity from multiple locations within the brain. Also, since light is used for measurements, the optrode does not generate heat or produce toxic byproducts, preventing tissue damage. The designed EO ring resonator exhibits a quality factor of approximately 10^4, allowing for the sensing of action potentials as small as 15 μV. Hence, the proposed method has the capability to overcome the limitations of current electrode-based methods, facilitating more accurate measurements of action potentials and advancing the understanding of neuronal activity in the brain.**

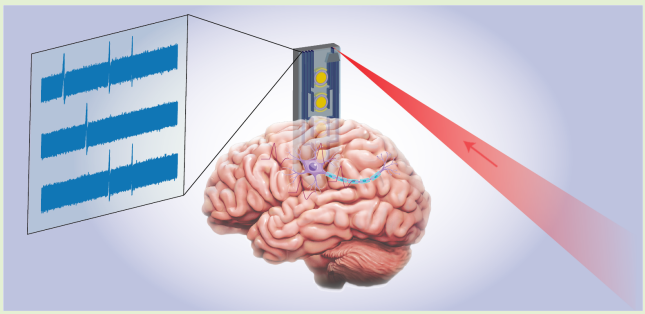

***Index Terms*—Electrooptic (EO) effect, lithium niobate, neuroprosthetics, optical modulators, optogenetics, ring resonator modulators, synaptic sensors.**

I. Introduction

In RECENT years, neuroscience research has made significant strides in studying the brain and the nervous system. Our understanding of the nervous system is further enhanced by utilizing cutting-edge sensor technologies that can deliver precise spatiotemporal information across extensive spatial domains. However, the precise measurement of action potentials, the electrical signals generated by neurons, with high spatiotemporal resolution remains a significant challenge. Since electrodes are well known for the measurement of electrical signals, the current approaches heavily rely on electrodes to measure action potentials and synaptic activities of neurons [1]. Two prominent electrode array technologies, namely, the Michigan and Utah arrays, have played a pivotal role in advancing our understanding of neural activities. The Michigan electrode array consists of a silicon-based platform with multiple shank electrodes, enabling simultaneous recording from multiple neurons with enhanced spatial resolution up to 35 electrodes/mm^2 [2]. On the other hand, the Utah electrode array features a flexible substrate (e.g., polyimide) and multiple penetrating electrode designs, allowing for precise and chronic neural recordings with a spatial resolution of up to 6 electrodes/mm^2 [3]. These cutting-edge electrode arrays represent significant advancements in neuroscience and hold promise for revolutionizing our understanding of brain function and its clinical applications. However, it is important to note that the relationship between the size of recording sites and impedance is inversely proportional, resulting in smaller electrodes being inherently noisier and displaying low recording quality. When dealing with weak signals, such as action potentials, obtaining recordings with minimal noise and

Manuscript received 16 April 2024; revised 14 May 2024; accepted 14 May 2024. Date of publication 22 May 2024; date of current version 1 July 2024. The associate editor coordinating the review of this article and approving it for publication was Dr. Emiliano Schena. *(Corresponding author: Ozdal Boyraz.)*

Ceren Babayigit and Ozdal Boyraz are with the Department of Electrical Engineering and Computer Science, University of California at Irvine, Irvine, CA 92697 USA (e-mail: cbabayig@uci.edu; oboyraz@uci.edu).

Rahim Esfandyarpour is with the Department of Electrical Engineering and Computer Science, the Department of Biomedical Engineering, and the Department of Mechanical and Aerospace Engineering, University of California at Irvine, Irvine, CA 92697 USA (e-mail: rahimes@uci.edu).

This article has supplementary downloadable material available at https://doi.org/10.1109/JSEN.2024.3402152, provided by the authors.

Digital Object Identifier 10.1109/JSEN.2024.3402152

high quality is crucial. Hence, the need for sensors with better performance and long-term stability is still open to investigation to be relevant to applications, such as brain–machine interfaces.

Optogenetics, calcium imaging, the use of voltage-sensitive labels, and electric-field (*E*-field) sensors are alternative approaches that can be used to measure action potentials. Optogenetics uses the response of genetically modified neurons to light. This modification enables their activation or inhibition through exposure to light, while simultaneously recording their responses [4]. Calcium imaging captures the changes in the concentration of calcium ions within cells to indirectly measure action potential [5]. In the case of voltage-sensitive dyes, changes in the electrical potential across the cell membrane labeled with voltage-sensitive markers are used as a direct method for monitoring neural activity [6]. Despite their advantages, these optical methods face limitations, such as restricted recording duration due to photobleaching, potential generation of phototoxic free radicals, and alterations in membrane electrical properties. Also, these approaches are not widely used in practice due to their complexity. On the other hand, *E*-field sensing is preferred for many healthcare monitoring due to its label-free nature, motion tolerance, and immunity to interference from other radio frequency (RF) services. If a proper probe design is provided, the same technique can be used for brain or tissue monitoring. According to Hales [7] and Cifra et al. [8], when an action potential occurs, it creates electromagnetic fields within the brain. This neuronal process causes membrane depolarization, resulting in ions' exit from the cell membrane. As these ions move, they generate ion currents that produce an electric field that is perpendicular to their direction of movement, in accordance with the right-hand rule. The detection of this electric field can be mapped to neural activities, as presented by Balch et al. [9].

In this work, we propose and investigate how to capture the *E*-field generated by synaptic activities by leveraging the electrooptic (EO) effect of lithium niobate ($LiNbO_3$). The ambient electric field will be weak, and the direction will be random. The EO effect, on the other hand, favors the *E*-field along certain orientations to induce a measurable phase change in the propagating optical field. Here, we investigate the method of detecting the weak *E*-field resulting from action potentials by sensing voltage variances in the extracellular medium. The proposed design pairs the unique EO properties of $LiNbO_3$ microring resonators (MRRs) with a coherent detection scheme (see Fig. 1) to capture synaptic activities in real time with μV voltage sensitivity and up to 249 electrodes/mm^2 spatial resolution. We show that single-neuron resolution imaging with a current detector output by capturing 15-μV action potentials, which corresponds to an *E*-field strength of 4.2 V/m. Diverging from traditional direct measurements of neural signals, the proposed design adeptly employs light modulation to convey the signal, which is subsequently processed through coherent detection. In essence, instead of relying on ambient *E*-fields, our method utilizes extracellular action potentials to create a strong, directional, and uniform *E*-field. This departure from ambient conditions ensures a more controlled and precise measurement

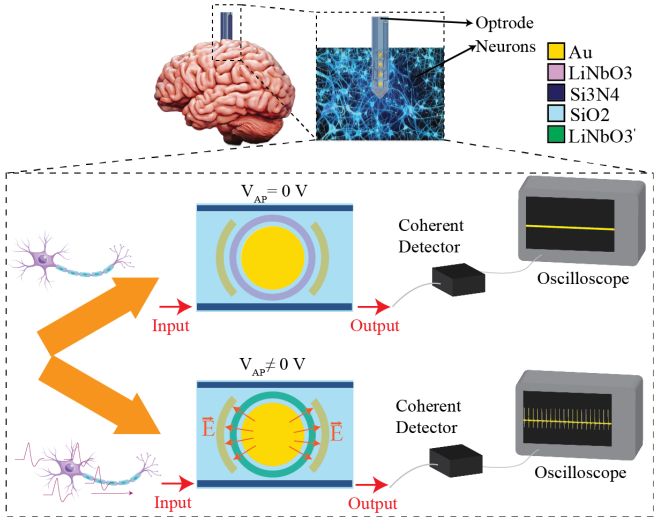

Fig. 1. Basic operating principle of the proposed optrode. Action potentials induce an electric-field creation across the $LiNbO_3$ waveguide and result in a refractive index change of $LiNbO_3$. This creates light modulation, which is extracted by the coherent detection to map electrical activity.

environment, distinct from the random directional variations present in ambient field measurements. This method allows for detecting subtle differences in the *E*-field generated by neurons, enabling us to record their activity without the need for exogenous labels. Furthermore, it mitigates susceptibility to electrical and biological noise, consequently reducing signal loss and enhancing sensitivity. This method could potentially pave the way for exploring the complex dynamics within neuronal networks, offering potential advancements in comprehending how the nervous system operates.

Up to date, optical *E*-field sensors (optrode) have been proposed as an alternative approach for conventional applications outside the biomedical field due to their benefits, such as minimal interference with the *E*-field being measured, the ability to measure a wide range of dynamic signals, a broad frequency response, and a high level of sensitivity. The fundamental operating mechanism of the most widely used optical *E*-field sensors is classified into two categories: the inverse piezoelectric effect [10] and the EO effect [11]. The inverse piezoelectric effect involves the generation of an *E*-field in response to mechanical stress or deformation of a material. In an optical *E*-field sensor based on this effect, a piezoelectric material is placed in an *E*-field, and the resulting mechanical deformation of the material is measured using an optical technique, such as interferometry. The magnitude of the *E*-field can be calculated based on the amount of deformation. On the other hand, the EO effect involves the modification of the refractive index of a material in response to an *E*-field exposure. In an optical *E*-field sensor based on this effect, a material with an EO coefficient is placed in an *E*-field, and the resulting change in the refractive index is measured. The magnitude of the *E*-field can be calculated based on the amount of refractive index change. EO effect *E*-field sensors are generally considered superior to piezoelectric effect *E*-field sensors due to their higher sensitivity, wider

dynamic range [12], higher linearity, and noninvasive nature, making them particularly suitable for applications requiring high precision.

Optical sensors based on the EO effect, such as the Mach–Zehnder interferometer, surface plasmon resonance sensors [13], fiber optic sensors, and MRR, have shown remarkable performance and potential for integration into photonic circuits. MRRs, in particular, have drawn considerable attention due to their compact size, high-quality factor (Q factor), and wavelength selectivity, making them ideal for a range of applications, including filtering, sensing, mode locking, EO modulation, optical memory, and optical switches [14], [15], [16], [17], [18], [19], [20]. In recent years, various material systems have been explored for MRR structures, including graphene [18], silicon, indium phosphide, polymer, and lithium niobate [21], [22], [23], [24]. Among these materials, $LiNbO_3$ has emerged as a promising candidate for E-field sensing applications, owing to its large linear EO coefficient, high modulation speed, and stable chemistry [25], [26]. In biosensing, $LiNbO_3$ ring resonators have primarily been utilized for detecting changes in the refractive index of surrounding materials, such as glucose [27], without tapping into the material's EO effect. However, our research departs from this trend by exploiting $LiNbO_3$'s EO properties to detect neural action potentials. Here, we present how we can utilize the large EO coefficient of $LiNbO_3$ for brain research and pave the way for further developments in brain–machine interfacing.

This article is organized as follows. In Section II, the structural design of the proposed $LiNbO_3$ MRR sensor and its operating principles are explored. Then, the temporal and spectral analyses of the proposed design are presented. Section III analyzes the insights into the signal modulation through the $LiNbO_3$ MRR structure. A possible experimental platform with the coherent detection scheme is given in Section IV along with detailed analyses of the probable action potential values. In Section V, we present multiarray designs, followed by a discussion (Section VI) on why EO resonators are feasible for the design while semiconductors are not. Finally, the summary of the study is provided in Section VII.

II. Design Approach and Principle of Operation

The MRR sensors are known to be excellent tools for capturing weak perturbations in the refractive index of the surrounding medium [15]. Here, we are not interested in the refractive index change of the surrounding material, but in capturing the refractive index changes in the sensor material due to neural activities. Also, resonant structures are known to be more sensitive to weak perturbations. Hence, we designed a synaptic sensor based on $LiNbO_3$ MRRs for high-sensitivity detection of the E-field generated by the action potential. The proposed optrode structure consists of a $LiNbO_3$ MRR on a silicon dioxide (SiO_2) substrate as a reliable and stable platform (see Fig. 2). The MRR structure has two gold electrodes to capture action potentials. The first electrode is buried in the SiO_2 layer and serves as a reference electrode. The second electrode, the inner gold plate, is exposed to neurons, and it captures the action potential and creates an electric field between the two electrodes, since it is in contact

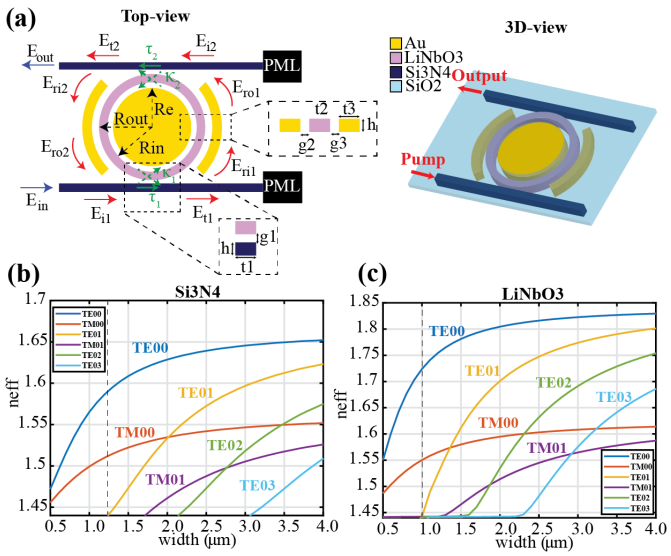

Fig. 2. (a) Schematic of EO ring resonator-based synaptic sensor. Mode analyses of (b) silicon nitride (Si_3N_4) and (c) lithium niobate ($LiNbO_3$) waveguides. Here, the height of the waveguides is set as 0.5 μm, and the width is swept from 0.5 to 4 μm.

with the surrounding medium and neurons to capture voltages created by neuron activities. The internal E-field induces a refractive index change in the $LiNbO_3$ waveguide sandwiched between two electrodes. This modulation of refractive index leads to modulation of the input light as it passes through the MRR structure, ultimately allowing for the detection of the electrical activity of neurons. The detection mechanism is a critical aspect of the optrode's design, and it employs a coherent detection system to achieve high sensitivity and accuracy. To assess the sensitivity of the proposed system, we built an analytical model based on an MRR sensor with a double-bus configuration, as shown in Fig. 2(a). Here, the corresponding outer radius of $LiNbO_3$ is adjusted as $R_{out} = 20$ μm. Dimensions are comparable to the size of a single neuron. Hence, it shows that such sensors have the capability of detecting single-cell activities, and potentially, they can achieve high spatial resolution. The in-and-out light coupling from the $LiNbO_3$ ring is performed by silicon nitride (Si_3N_4) bus waveguides.

To operate in a single mode, the widths of the $LiNbO_3$ and Si_3N_4 bus waveguides are determined using finite-difference time-domain (FDTD) mode analyses shown in Fig. 2(b) and (c) by using Lumerical simulation tool. The optimized width of the $LiNbO_3$ waveguide, which yields the highest Q factor in single mode, is found to be $t_2 = 0.63$ μm, while the widths of Si_3N_4 bus waveguides are set as $t_1 = 1$ μm. As a result, we obtained the inner radius as $R_{in} = 19.37$ μm. To achieve optimal coupling between the waveguides, the gap between the $LiNbO_3$ waveguide and the Si_3N_4 bus waveguides is set to $g_1 = 0.15$ μm. The inner gold plate, which is in contact with the exterior medium, has a radius of $R_e = 17.87$ μm that leaves 1.5-μm spaces (g_2) between the $LiNbO_3$ waveguides. The outer gold plate, which serves as the reference, has a thickness of $t_3 = 2$ μm with a spacing of $g_3 = 1.5$ μm from the $LiNbO_3$ waveguide. Furthermore, the thickness of

the structure is set as $h = 0.5$ μm for all components. It has been previously demonstrated that the fabrication of $LiNbO_3$ is attainable within a thickness range spanning from 400 to 900 nm [28], [29], [30]. Finally, to ensure that unwanted interference or distortion does not occur, the unused ends of the waveguides can be coated with perfectly matched layers (PMLs) or tapered.

The main sensor architecture is an add-drop filter consisting of two waveguides situated on opposite sides of a ring resonator, as illustrated in Fig. 2(a). The function of the lower the one waveguide is to introduce light into the resonators, while the upper waveguide is responsible for extracting light from the resonator. The optical resonance can be observed at two output ports. The pass port, located at the opposite end of the input port, is the first waveguide in the add-drop structure. At the resonance wavelength, a dip in the transmission is observed in the pass port. The drop port, serving as the second output in the add-drop structure, exhibits a reverse transmission response compared to the add port. It demonstrates transmission peaks at the resonant wavelengths.

The static transmission to both the pass port and the drop port can also be represented for continuous wave (CW) operation by matching the fields as follows [31], [32]:

$$T_{\text{pass}} = \frac{I_{\text{pass}}}{I_{\text{input}}} = \frac{\tau_2^2 a^2 - 2\tau_1\tau_2 a\cos(\theta) + \tau_1^2}{1 - 2\tau_1\tau_2 a\cos(\theta) + (\tau_1\tau_2 a)^2} \quad (1)$$

$$T_{\text{drop}} = \frac{I_{\text{drop}}}{I_{\text{input}}} = \frac{(1-\tau_2^2)(1-\tau_1^2)a}{1 - 2\tau_1\tau_2 a\cos(\theta) + (\tau_1\tau_2 a)^2} \quad (2)$$

where θ is the phase shift of the light after one round trip inside the ring, a is the amount of attenuation of light after one round trip, and τ_i is the self-coupling coefficient between $LiNbO_3$ ring and Si_3N_4 waveguides.

For illustration purposes, here, we present analysis based on signal reading at the drop port. The FDTD simulations are performed utilizing the parameters specified in Section II, followed by the transmission measurement at the drop port. The observed spectral response of the MRR sensor is represented in Fig. 3(a). The transmission peaks exhibit a free spectral range (FSR) of 0.9440 THz and a Q factor of 8.9756×10^3. To see resonance mode transmission through the drop port, cross-sectional intensity field distributions along the xy plane are represented in Fig. 3(b) and (c) for the selected frequency values of $f = 192.5$ THz (point A) and $f = 193.906$ THz (point B). The labeled letters superimposed in Fig. 3(a) indicate the frequency location in the transmission spectrum of the MRR. As expected, a noticeable enhancement in intensity is observed at the drop port when reaching the resonance point (referred to as B). Rather than operating at the resonance point, this proposed approach will bias the laser at the linear point of the transmission peak. This strategy aims to achieve a more sensitive response in detecting refractive index changes induced by the E-field. To determine this point, the derivative of the transmission peak centered at $f = 193.906$ THz is calculated and depicted in Fig. 3(d). Here, the point, C, corresponding to $f = 193.951$ THz is the linear point that gives the highest change in the transmission output. Since the MRR is biased at the quadrature point, the drop-port intensity is also at its midpoint, as shown in Fig. 3(e).

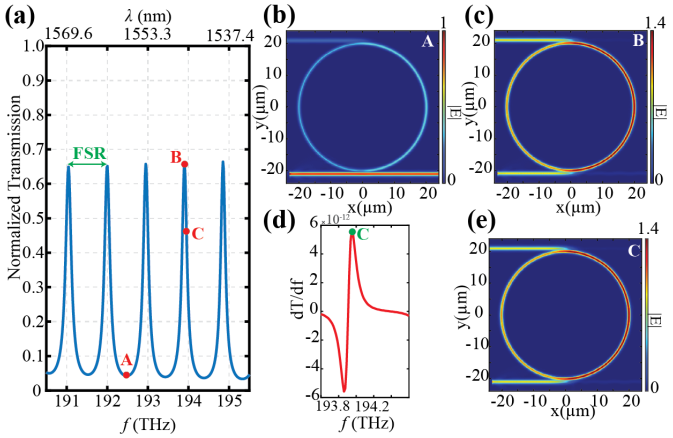

Fig. 3. (a) Transmission spectra of the synaptic sensor. Steady-state electric-field intensity distributions for (b) at $f = 192.5$ THz (point A) and (c) at $f = 193.906$ THz (point B). (d) Derivative of the transmission spectra with respect to frequency for a focus range. (e) Electric-field intensity distributions for the bias point at $f = 193.951$ THz (point C).

III. Signal Modulation via $LiNbO_3$ MRR

The ring resonator steady-state transfer function is derived theoretically by describing the relation between electromagnetic waves in the straight waveguides before and after coupling regions (see Fig. 2). We have two coupling regions, which are modeled by coupling matrices as follows:

$$\begin{bmatrix} E_{t1} \\ E_{ri1} \end{bmatrix} = \begin{bmatrix} \tau_1 & i\kappa_1 \\ i\kappa_1 & \tau_1 \end{bmatrix} \begin{bmatrix} E_{i1} \\ E_{ro1} \end{bmatrix} \quad (3)$$

$$\begin{bmatrix} E_{t2} \\ E_{ri2} \end{bmatrix} = \begin{bmatrix} \tau_2 & i\kappa_2 \\ i\kappa_2 & \tau_2 \end{bmatrix} \begin{bmatrix} E_{i2} \\ E_{ro1} \end{bmatrix} \quad (4)$$

where the amplitude cross-coupling and self-coupling coefficients are given by κ_i and τ_i, respectively, and $|\kappa_i|^2 + |\tau_i|^2 = 1$. Note that the cross-coupling and self-coupling coefficients for both ports are identical; hence, they can be represented as $\kappa = \kappa_1 = \kappa_2$ and $\tau_i = \tau_1 = \tau_2$. After generating the input wave, a fraction of it is coupled into the resonator to form a traveling wave that circulates clockwise around the ring. During a single round trip around the ring, the circulating wave experiences attenuation due to intrinsic optical losses. The attenuation factor can be expressed as $a^2 = \exp(-\alpha L)$, where α is the attenuation coefficient in the ring and L is the total circumference of the ring. The traveling wave that circulates in a clockwise direction around the ring also undergoes a phase shift, denoted by θ, which can be expressed as $\theta = \omega T$, where ω represents the angular frequency of the input field and T is the round-trip travel time of the ring. The round-trip travel time, denoted by T, is given by $T = nL/c$, where n is the effective refractive index of the ring, L is the ring's circumference, and c represents the vacuum light speed. In the case of $LiNbO_3$, the material's refractive index varies depending on the electric field induced by the neurons. Hence, it can be shown as $n(V(t)) = (n_0 - (1/2)n_0^3 r_{13}(V(t)/d))$, where d is the spacing between the electrodes, n_0 is the effective refractive index of the propagating mode, and r_{13} is the EO coefficient of the $LiNbO_3$. Then, the phase shift can be rewritten as follows $\theta(t) = 2\pi/\lambda n(V(t))L$. By using the given relations, the static field transfer function of the double-bus

MRR system for the drop port can be written as follows:

$$\frac{E_{\text{out}}}{E_{\text{in}}} = \frac{-(1-\tau^2)\sqrt{a}e^{j\theta(t)/2}}{\tau(1-ae^{j\theta(t)})}. \quad (5)$$

Optical modulation in a microring resonator is accomplished by modulating the refractive index of the resonator, which can be achieved by varying the applied voltage $V(t)$ or, equivalently, the effective refractive index $n(t)$. The action potential induced by the neurons produces a time-varying refractive index modulation, which gives rise to intensity modulation in the output of the resonator. Hence, the dynamic transfer function of the MMR is essential for characterizing its response to time-varying input signals. The dynamic transfer function of the MMR provides information on how the resonator responds to changes in its input signal, including changes in frequency and amplitude. If we define the static output signal as follows:

$$s_{\text{out}}(t) = E_{\text{in}}\frac{-(1-\tau^2)\sqrt{a}e^{j\theta(t)/2}}{\tau(1-ae^{j\theta(t)})}. \quad (6)$$

Then, we can define the output signal after the dynamic response as follows:

$$s_{\text{out}_{\text{dynamic}}}(t) = A_{\text{in}}\big[\cos(2\pi f_{\text{in}}t) + m\cos(2\pi f_m t + \phi_m)\cos(2\pi f_{\text{in}}t)\big] \quad (7)$$

where $m(t) = (|s_{\text{out}}(t)|/A_{\text{in}})$. Thus, the time-varying signal at the end of the drop port, after the modulation induced by the action potential, is defined by (7). By solving it, we can accurately predict the response of the $LiNbO_3$ ring resonator to the action potential.

IV. Potential Experimental Scenario With Coherent Detection

The optical characterization of the proposed system can be carried out via coherent detection of the modulated signal within the experimental scenario illustrated in Fig. 4(a). We start with a laser beam that is split into two branches: the signal beam and the reference or local oscillator beam. Subsequently, the signal beam is coupled to the waveguide and resonator. As a result, the resonator will experience the modulation induced by the neuron action potential as defined in (7) and generate the E-field presented in (S1). The modulated signal is then coupled out of the resonator and directed to the coherent detection system. The unmodulated reference beam with an E-field profile in (S2) is directed onto the coherent detection system where the reference beam acts as a local oscillator. The interfering signal beam and the local oscillator signal are then converted to photocurrent by a balanced detector. The resultant differential photocurrent generated by the matched detectors can be expressed as follows [33]:

$$I(t) = 2R\sqrt{P_{\text{in}}P_{\text{lo}}}\cos(\phi_{\text{in}}+\phi_{\text{lo}}) + m\cos(2\pi f_m t + \phi_m + \phi_{\text{in}} + \phi_{\text{lo}}). \quad (8)$$

By beating the modulated signal induced by the action potential with the reference signal, the system can accurately detect and quantify the neural activity. The literature reports that action potentials generated by neurons typically exhibit an amplitude ranging from 30 μV to 100 mV and a period in the range of 0.6–0.1 s (see Table I). Based on the reported amplitude and frequency range of action potentials in the literature, we conducted a comprehensive analysis of detectability of the neural activities. In our initial analysis, we focus on assessing the signal-to-noise ratio (SNR) of the generated electrical signal for different optical power values and under 30-μV action potential excitation. For this study, we limit the detection (noise) bandwidth (BW) to 1 kHz, and we set the relative intensity noise (RIN) of the laser at a constant level of -160 dB/Hz. The SNR calculations include the shot noise and thermal noise generated by the detector and the RIN of the source laser as described in (9). The phase noise of the laser and the dark current are ignored in this case

TABLE I
Amplitude and Period Information of Action Potentials of Different Kinds of Neuron Cells

Ref.	Cell Type	Period	Amplitude
[36]	Hippocampal neurons	1.5-2.5 ms	100-200 μV
[37]	Monkey's Inhibitory cells	0.2-1 ms	30-100 mV
[38]	Mammalian central neurons	2 ms	20-40 mV
[39]	hiPSC-CM	0.1 s	3.56 mV
[40]	neocortex of rats	0.7 ms	120 μV
[41]	neurons in the nucleus laminarins	2 ms	8.38 mV
[42]	hippocampal neurons from postnatal mice	0.6 ms	30-50 μV

$$\text{SNR} = \frac{I^2}{\sigma_S^2+\sigma_T^2+\sigma_{RIN}^2} = \frac{I^2}{2qRP_{\text{avg}}\Delta F + \frac{4K_BT}{R_L}\Delta F + (RP_{\text{avg}})^2 10^{\text{RIN}(f,P_{\text{avg}})/10}\Delta F}$$

$$\text{where} \quad \text{RIN}(f, P_{\text{avg}}) = \frac{S_{\delta P}(f)}{P_{\text{avg}}^2}. \quad (9)$$

Here, q is the electron charge, ΔF is the electrical detection BW or noise BW, K_B is Boltzmann's constant, T is the temperature (K), R_L is the load resistance, $S_\delta P(f)$ is the power spectral density, f is the frequency, and RIN (in linear scale) is the RIN of the laser. It is important to know that increasing the pump's power can make the laser more stable and reduce the RIN in its output. So, practical scenarios may yield more favorable outcomes than those predicted by a simplistic linear assumption [34], [35].

Fig. 4(b) illustrates a mesh plot depicting the SNR levels across a range of input and local oscillator power settings. Due to the power-dependent nature of shot noise and RIN, it becomes evident that by amplifying the local oscillator power, the system becomes RIN-dependent, and SNR will decrease in the simplistic model mentioned above. For local oscillator powers less than 2 mW, it is more shot noise-dependent, and SNR improves with the local oscillator power. For a clearer demonstration of this characteristic, cross sections have been extracted from the mesh plot at the specific input powers of 0.2, 0.4, 0.6, 0.8, and 1 mW, as indicated in Fig. 4(c). In a subsequent analysis, the input power was fixed at 1 mW, and the noise variances for thermal noise

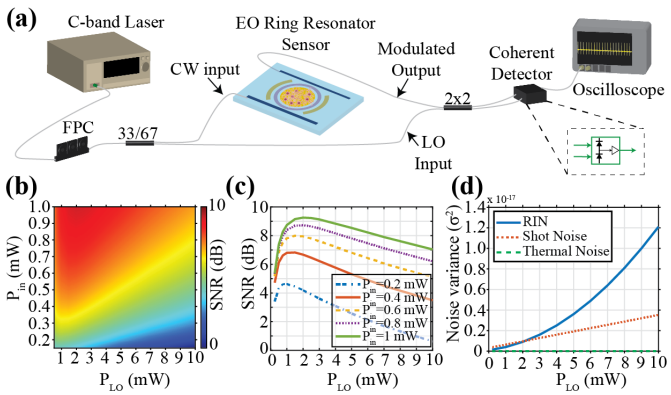

Fig. 4. (a) Schematic of the experimental scenario. (b) Mapping SNR in a plane (P_{lo} and P_{in}) at 30-μV action potential amplitude. (c) Cross sections extracted from the SNR map for different input power values. (d) Noise characteristics of the system for P_{in} = 1-mW input power.

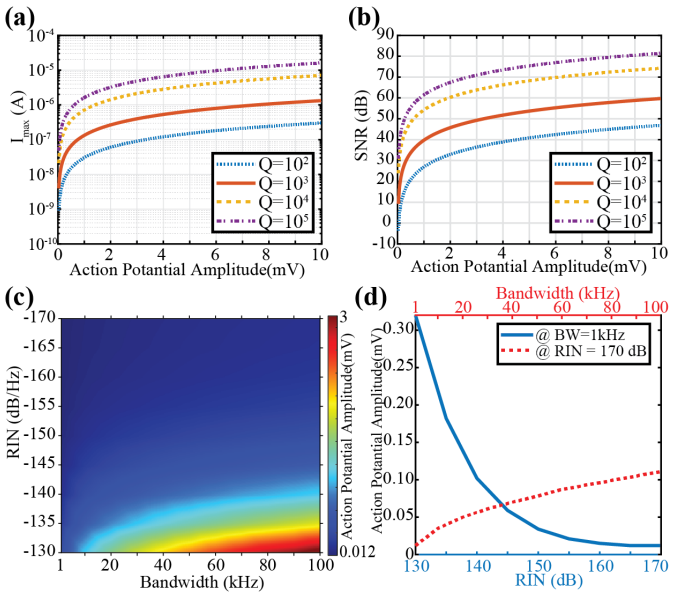

Fig. 5. (a) Variations in output current obtained via coherent detection relative to action potential amplitude for different Q-factor values. (b) Calculated SNR values of the system relative to action potential amplitude, with variations in Q-factor values. (c) Mapping detectable action potential amplitude in a plane (BW and RIN) at 3-dB SNR. (d) Cross sections extracted from the amplitude map at BW = 1 kHz and RIN = −170 dB/Hz.

shot noise and RIN were plotted while varying the local oscillator power. As depicted in Fig. 4(d), it is evident that up to 2 mW, the system is limited by shot noise, whereas beyond 2 mW, the system becomes limited by RIN. Hence, due to the quadratic relationship between RIN and power, once the system transitions to being RIN-limited, the SNR experiences a rapid and pronounced decrease, as seen in Fig. 4(c). Following this comprehensive analysis, a fixed input power of 1 mW and a local oscillator power of 2 mW were identified as the optimal settings for subsequent analyses, as they resulted in the highest SNR values.

In our next analysis, we focus on assessing the SNR of the generated electrical signal for different values of action potential captured by the probe. This assessment is carried out by varying amplitude levels of the action potential from 30 μV to 100 mV while maintaining a constant period of 1 ms. To assess the impact of the Q values of the ring resonator, we vary the Q values from 10^2 to 10^5 in the same analysis. Here, we assume the optical power of the local oscillator at 2 mW at the input of the 2 × 2 coupler, and the average signal power at the resonator input is 1 mW. After passing through the ring resonator, the power observed at the input arm of the 2 × 2 coupler is 0.69 mW. As depicted in Fig. 5(a) and (b), we observe that the sensor's sensitivity increased as the Q-factor value increased. The output current exhibited a range spanning from nanoamps to milliamps, demonstrating the sensor's ability to detect action potentials across a wide amplitude spectrum. Notably, Q factors greater than 10^2 can detect action potentials with amplitudes as small as 30 μV. In cases where the Q factor was equal to 10^2, the 3-dB SNR is achievable at 65-μV action potentials at the sensor. The same level of action potential at the sensor can generate 37-dB SNR if a ring resonator with $Q = 10^5$ is used. The 30-μV action potential is detectable with 9-dB SNR if a ring resonator with a Q of 10^3 is used. If we seek 24-dB SNR, we need to work with the ring resonator having a Q of 10^4.

Next, we have conducted a study on the impact of laser RIN on the detectability of the action potential. Here, we assume that the optical power levels are the same as before, and the Q value of the resonator is assumed to be $Q = 10^3$. We investigate maximum tolerable laser RIN to achieve 3-dB SNR at the detector. In practice, the detector BWs are larger than 100 MHz. However, since our signal is in the order of 1 kHz, we limit the noise BW to up to 100 kHz in our analyses. Fig. 5(c) presents the mesh plot of 3-dB SNR for various detection BWs and RIN. As shown in the figure, a narrow linewidth laser is with an RIN value of −160 dB/Hz, and a 3-dB SNR is achievable at ∼15-μV and ∼147-μV action potentials by using detection BWs of 1 and 100 kHz, respectively. By using a typical telecom grade DFB laser with −145-dB/Hz RIN value, 3-dB SNR is achievable at 60-μV action potentials with a detection BW of 1 kHz. In the case of a 100-kHz detection BW, the 3-dB SNR can be reached at approximately 580-μV action potentials.

Fig. 5(d) presents the required RIN values and action potentials to achieve 3-dB SNR at different detection BWs. As shown with the solid blue curve, ∼47-μV action potential is detectable if the noise BW is 10 kHz by using a −160-dB/Hz RIN value, while ∼185-μV action potential is detectable by using a −145-dB/Hz RIN at the same BW. Also, we present minimum detectable action potential for various noise BW values by using an ultranarrow linewidth laser with −170-dB/Hz linewidth. In this case, the detectable amplitude values exhibit a range from ∼12 to ∼110 μV within a detection BW that ranges from 1 to 100 kHz.

From the outcomes of the aforementioned analyses, it is clear that one can tailor the sensor parameters to suit specific application requirements. As presented in Table I, action potentials and their periods vary for different neuron

types. Hence, depending on the targeted application, the required sensitivity and noise BWs change. For instance, while 1-kHz noise BW and 200-μV sensitivity are necessary for hippocampal neurons, mammalian central neurons can deliver as much as 20-μV action potential with 1-kHz synapse rates. Since the proposed system has a large dynamic range, it can be adapted to desired applications. This finding underscores the potential of the microring resonator sensor with coherent detection as a promising tool for the precise and accurate measurement of neural activity in various applications, including but not limited to neuroscience research, clinical diagnostics, and brain–machine interfaces.

V. Array Configuration With $LiNbO_3$ MMR

One type of neural probe that has gained significant attention in recent years is the multiarray electrode (MAE). MAEs are highly advanced devices that consist of an array of microelectrodes capable of simultaneously recording or stimulating neural activity from multiple locations within the brain. By recording the activity of large populations of neurons simultaneously, researchers can obtain a more comprehensive understanding of the brain's activity patterns and dynamics. In addition, the ability to stimulate neural activity in precise patterns and locations using MAEs has opened up new possibilities for developing treatments for neurological disorders, such as epilepsy and Parkinson's disease [43]. Several well-known MAEs have been developed over the years, including the Utah array [3] and the Michigan probe [2]. One challenge with the Utah and Michigan array is that the spacing between the microelectrodes is relatively large (400 μm and 100 μm, respectively) compared to the size of individual neurons, which can limit the spatial resolution of recordings [44]. MAE systems, including the Utah and Michigan probes, also suffer from some noise in their recorded signals due to the use of wires to carry the electrical signals. Several sources of noise can affect the signals recorded by these probes, including electrical noise and signal attenuation. Electrical noise can come from a variety of sources, including power lines, electronic devices, and even the body's electrical activity, and it can interfere with the small signals recorded by the electrodes, making it more difficult to extract meaningful information. Also, the electrical signals recorded by the electrodes can weaken, as they travel through the wires, leading to a loss of signal strength and fidelity. To address these challenges, we propose an array structure with $LiNbO_3$ MRRs, which has a 20-μm diameter and 50-μm spacing distance, as shown in Fig. 6(a) and (b). Since the proposed system uses the modulated optical signal to carry information rather than carrying the weak signal over a wire, it is more susceptible to noise and signal attenuation. Another important parameter for spatial resolution is the density of the electrodes. The commonly used Utah array typically includes 96 electrodes on a single array covering an area of 4 × 4 mm [45]. On the other hand, the Michigan array includes 64 electrodes on a single array covering an area of 0.6 × 3 mm [40]. We propose the use of a single array containing 400 electrodes, which covers an area of 1.64 × 0.977 mm. This array is shown schematically in Fig. 6(b) in a one-row configuration. The spacing between

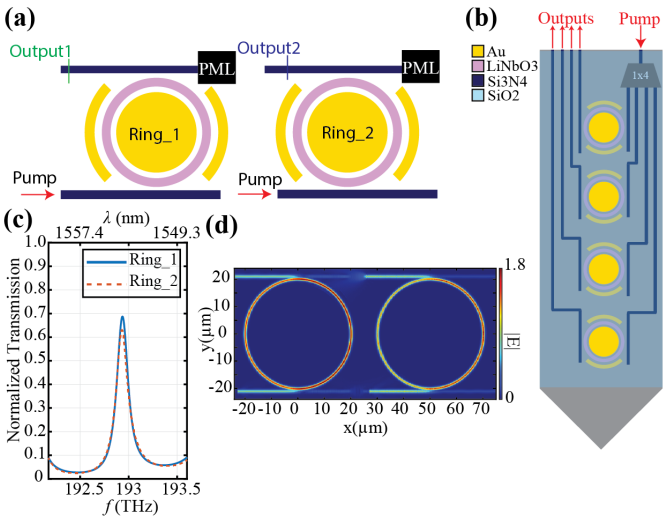

Fig. 6. (a) Schematic of EO ring resonator-based synaptic sensor in an array configuration. (b) Schematic of optrode with array configuration. (c) Transmission spectra of the array configuration. (d) Steady-state electric-field intensity distributions at $f = 192.938$ THz.

the Si_3N_4 waveguides is taken as 500 nm, which is specified in [46].

Upon conducting 3-D FDTD analyses for the array configuration depicted in Fig. 6(c) and (d), we observed that both ring resonators with a spacing of 50 μm demonstrated identical responses at the same resonant frequency. This finding suggests that the proposed configuration may offer enhanced scalability and potential for multiplexed sensing applications, where multiple sensors can be arranged in an array format to enable simultaneous detection of multiple signals in parallel. The main drawback of the system is the power consumption, primarily due to the splitting of input power and the local oscillator into multiple paths ($1 \times N$ configuration).

VI. Discussion

The design of the MRR can also be conducted by using semiconductor material, such as silicon (Si). Silicon ring resonators play a crucial role in the field of photonics and integrated optics, since their integration with other photonic components on a CMOS platform enables miniaturization and cost reduction, making them practical and scalable. With high-Q factors and the ability to sustain resonant modes, silicon ring resonators ensure efficient light interaction and enhance sensitivity. However, due to the centrosymmetric crystal structure of Si, it does not exhibit a linear EO effect (Pockels). Soref and Bennet [47] have conducted investigations on E-field effects in Si to assess their effectiveness, and it has shown that the Kerr effect [48], [49], [50] and the Franz–Keldysh effect are small in Si, too. Hence, to be able to obtain modulation in Si MRR, one should use the carrier depletion effect [47]. In this configuration, the ring resonator is biased in the depletion mode, creating a depletion region within the waveguide of the ring. This depletion region alters the effective refractive index of the waveguide, making it sensitive to changes in the E-field applied. When an external E-field is applied to the sensor, it modifies the width and depth of the depletion region, leading to a change in the effective refractive index of the waveguide. This change affects the resonance properties of the ring resonator.

Nevertheless, there are two main drawbacks to that configuration, which make $LiNbO_3$ more suitable for the proposed sensor design rather than Si. First, temperature fluctuations can affect the performance of these sensors due to their reliance on the carrier concentration and dimensions of the depletion region. Temperature variations can alter the properties of the depletion region, leading to changes in the sensor's response and potentially introducing inaccuracies in the measured *E*-field. In [51], it has been demonstrated that brain temperature is not stable within the normal physiological and behavioral continuum but rather shows relatively large fluctuations (2 °C–4 °C). Hence, to mitigate this issue, temperature compensation techniques or additional temperature sensors may be required to ensure accurate and reliable measurements. Second, depletion mode sensors require a continuous bias voltage to maintain the depletion region, resulting in continuous power consumption. The biasing conditions must be carefully addressed to achieve optimal performance. Moreover, it requires additional cabling in the design to sustain the biasing. Thus, while semiconductor materials, such as silicon, may exhibit promising quality factor values, their practical limitations make them less conducive to certain applications, such as action potential measurements. In this direction, with its high EO coefficient, $LiNbO_3$ is preferred to be used in the proposed design to illustrate the potential of EO crystals in neuroscientific research.

VII. Conclusion

In conclusion, this study presents a novel optrode design that utilizes the EO effect of $LiNbO_3$ to enable highly sensitive and precise measurement of action potentials in neuroscience research. The proposed optrode combines the EO effect with a ring resonator and coherent balance detector, allowing for the detection of subtle changes in the refractive index induced by neuronal activity. The optrode offers several advantages over current electrode-based methods, including enhanced spatial resolution, decreased susceptibility to biological interference, and heightened sensitivity to faint signals. Furthermore, the optical aspect of the optrode provides operational flexibility in terms of wavelength, allowing for versatility in experimental setups. Moreover, its label-free nature and compact size enable seamless integration into multichannel sensing configurations, enhancing its applicability in multiplexed sensing applications. By leveraging the EO properties of $LiNbO_3$, the opto-probe can detect changes in the *E*-field on the order of picometers with a temporal resolution in the nanosecond range. Furthermore, the use of light for measurements eliminates the generation of heat and toxic byproducts, ensuring the safety of the tissue being measured. The analytical and numerical results demonstrate the feasibility and performance of the proposed optrode, with high-quality factor MRRs and high sensitivity to microvolt-level signals. Overall, the findings of this research contribute to the development of a new tool that overcomes the limitations of current electrode-based methods, enabling more accurate and precise measurements of action potentials and providing insights into the intricate dynamics of neuronal networks.

References

[1] G. Hong and C. M. Lieber, "Novel electrode technologies for neural recordings," *Nature Rev. Neurosci.*, vol. 20, no. 6, pp. 330–345, Jun. 2019.

[2] K. D. Wise, D. J. Anderson, J. F. Hetke, D. R. Kipke, and K. Najafi, "Wireless implantable microsystems: High-density electronic interfaces to the nervous system," *Proc. IEEE*, vol. 92, no. 1, pp. 76–97, Jan. 2004.

[3] P. K. Campbell, K. E. Jones, R. J. Huber, K. W. Horch, and R. A. Normann, "A silicon-based, three-dimensional neural interface: Manufacturing processes for an intracortical electrode array," *IEEE Trans. Biomed. Eng.*, vol. 38, no. 8, pp. 758–768, Aug. 1991.

[4] F. Atry et al., "Monitoring cerebral hemodynamics following optogenetic stimulation via optical coherence tomography," *IEEE Trans. Biomed. Eng.*, vol. 62, no. 2, pp. 766–773, Feb. 2015.

[5] C. Grienberger, A. Giovannucci, W. Zeiger, and C. Portera-Cailliau, "Two-photon calcium imaging of neuronal activity," *Nature Rev. Methods Primers*, vol. 2, no. 1, pp. 1–23, 2022.

[6] R. W. Pak, J. Kang, E. Boctor, and J. U. Kang, "Optimization of near-infrared fluorescence voltage-sensitive dye imaging for neuronal activity monitoring in the rodent brain," *Frontiers Neurosci.*, vol. 15, Oct. 2021, Art. no. 742405.

[7] C. G. Hales, "The origins of the brain's endogenous electromagnetic field and its relationship to provision of consciousness," *J. Integrative Neurosci.*, vol. 13, no. 2, pp. 313–361, Jun. 2014.

[8] M. Cifra, J. Z. Fields, and A. Farhadi, "Electromagnetic cellular interactions," *Prog. Biophys. Mol. Biol.*, vol. 105, no. 3, pp. 223–246, May 2011.

[9] H. B. Balch et al., "Graphene electric field sensor enables single shot label-free imaging of bioelectric potentials," *Nano Lett.*, vol. 21, no. 12, pp. 4944–4949, Jun. 2021.

[10] M. Cheng et al., "A high-resolution electric field sensor based on piezoelectric bimorph composite," *Smart Mater. Struct.*, vol. 31, no. 2, Feb. 2022, Art. no. 025008.

[11] M. Luo, Q. Yang, F. Dong, N. Chen, and W. Liao, "Miniature micro-ring resonator sensor with electro-optic polymer cladding for wide-band electric field measurement," *J. Lightw. Technol.*, vol. 40, no. 8, pp. 2577–2584, Apr. 2022.

[12] X. Ma, C. Zhuang, R. Zeng, and W. Zhou, "Large-dynamic-range athermal lithium niobite on insulator/TiO_2 nanobeam electric field sensor," *J. Phys. D, Appl. Phys.*, vol. 54, no. 10, Mar. 2021, Art. no. 105101.

[13] M. W. Khan and O. Boyraz, "Polarization-sensitive terahertz bolometer using plasmonically-heated vanadium-dioxide beam," *Int. J. Thermophys.*, vol. 44, no. 1, p. 9, Jan. 2023.

[14] A. K. Seyfari, M. Bahadoran, and P. Yupapin, "Design and modeling of double panda-microring resonator as multi-band optical filter," *Nano Commun. Netw.*, vol. 29, Sep. 2021, Art. no. 100352.

[15] C. Liu, C. Sang, X. Wu, J. Cai, and J. Wang, "Grating double-slot micro-ring resonator for sensing," *Opt. Commun.*, vol. 499, Nov. 2021, Art. no. 127280.

[16] C. Babayigit, C. Boztug, H. Kurt, and M. Turduev, "Fabry–Pérot microtube cavity structure for optical sensing at mid-infrared spectrum," *IEEE Sensors J.*, vol. 20, no. 5, pp. 2390–2397, Mar. 2020.

[17] M. Yu et al., "Raman lasing and soliton mode-locking in lithium niobate microresonators," *Light, Sci. Appl.*, vol. 9, no. 1, p. 9, Jan. 2020.

[18] Y. Wang, L. Lei, J. Zang, W. Dong, X. Zhang, and P. Xu, "High efficiency electro-optic modulation in a graphene silicon hybrid tapered microring resonator," *IEEE Access*, vol. 9, pp. 87869–87876, 2021.

[19] A. A. Nikitin et al., "Optical bistable SOI micro-ring resonators for memory applications," *Opt. Commun.*, vol. 511, May 2022, Art. no. 127929.

[20] M. K. Chhipa, B. T. P. Madhav, and B. Suthar, "An all-optical ultracompact microring-resonator-based optical switch," *J. Comput. Electron.*, vol. 20, no. 1, pp. 419–425, Feb. 2021.

[21] Y. Yuan, W. V. Sorin, Z. Huang, D. Liang, M. Fiorentino, and R. G. Beausoleil, "A 100 Gb/s PAM4 two-segment silicon microring resonator modulator," in *Proc. IEEE Photon. Conf. (IPC)*, Oct. 2021, pp. 1–2.

[22] R. R. Kumar, M. Raevskaia, V. Pogoretskii, Y. Jiao, and H. K. Tsang, "Entangled photon pair generation from an InP membrane micro-ring resonator," *Appl. Phys. Lett.*, vol. 114, no. 2, Jan. 2019, Art. no. 021104.

[23] F. Qiu and Y. Han, "Electro-optic polymer ring resonator modulators [invited]," *Chin. Opt. Lett.*, vol. 19, no. 4, 2021, Art. no. 041301.

[24] M. Zhang et al., "Broadband electro-optic frequency comb generation in a lithium niobate microring resonator," *Nature*, vol. 568, no. 7752, pp. 373–377, Apr. 2019.

[25] E. H. Turner, "High-frequency electro-optic coefficients of lithium niobate," *Appl. Phys. Lett.*, vol. 8, no. 11, pp. 303–304, 1966.

[26] E. L. Wooten et al., "A review of lithium niobate modulators for fiber-optic communications systems," *IEEE J. Sel. Topics Quantum Electron.*, vol. 6, no. 1, pp. 69–82, Jan. 2000.

[27] M. A. Uddin, M. M. S. Maswood, U. K. Dey, A. G. Alharbi, and M. Akter, "A novel optical micro ring resonator biosensor design using lithium niobate on insulator (LNOI) to detect the concentration of glucose," in *Proc. 2nd Novel Intell. Lead. Emerg. Sci. Conf. (NILES)*, Oct. 2020, pp. 350–354.

[28] J. Zhang et al., "An ultra-high-Q lithium niobate microresonator integrated with a silicon nitride waveguide in the vertical configuration for evanescent light coupling," *Micromachines*, vol. 12, no. 3, p. 235, 2021.

[29] P. Rabiei and W. H. Steier, "Lithium niobate ridge waveguides and modulators fabricated using smart guide," *Appl. Phys. Lett.*, vol. 86, no. 16, Apr. 2005, Art. no. 161115.

[30] P. Rabiei, J. Ma, S. Khan, J. Chiles, and S. Fathpour, "Heterogeneous lithium niobate photonics on silicon substrates," *Opt. Exp.*, vol. 21, no. 21, p. 25573, Oct. 2013.

[31] W. Bogaerts et al., "Silicon microring resonators," *Laser Photon. Rev.*, vol. 6, no. 1, pp. 47–73, Jan. 2012, doi: 10.1002/lpor.201100017.

[32] A. Sarkaleh, B. Lahijani, H. Saberkari, and A. Esmaeeli, "Optical ring resonators: A platform for biological sensing applications," *J. Med. Signals Sensors*, vol. 7, no. 3, p. 185, 2017.

[33] M. Seimetz, *High-Order Modulation for Optical Fiber Transmission*. Cham, Switzerland: Springer, 2009.

[34] B.-B. Zhao, X.-G. Wang, J. Zhang, and C. Wang, "Relative intensity noise of a mid-infrared quantum cascade laser: Insensitivity to optical feedback," *Opt. Exp.*, vol. 27, no. 19, p. 26639, Sep. 2019.

[35] Y. Deng, B.-B. Zhao, Y.-T. Gu, and C. Wang, "Relative intensity noise of a continuous-wave interband cascade laser at room temperature," *Opt. Lett.*, vol. 44, no. 6, p. 1375, Mar. 2019.

[36] Y. Nam, J. C. Chang, B. C. Wheeler, and G. J. Brewer, "Gold-coated microelectrode array with thiol linked self-assembled monolayers for engineering neuronal cultures," *IEEE Trans. Biomed. Eng.*, vol. 51, no. 1, pp. 158–165, Jan. 2004.

[37] L. S. Krimer et al., "Cluster analysis-based physiological classification and morphological properties of inhibitory neurons in layers 2–3 of monkey dorsolateral prefrontal cortex," *J. Neurophysiol.*, vol. 94, no. 5, pp. 3009–3022, 2005.

[38] B. P. Bean, "The action potential in mammalian central neurons," *Nature Rev. Neurosci.*, vol. 8, no. 6, pp. 451–465, Jun. 2007.

[39] M. Dipalo et al., "Intracellular action potential recordings from cardiomyocytes by ultrafast pulsed laser irradiation of fuzzy graphene microelectrodes," *Sci. Adv.*, vol. 7, no. 15, Apr. 2021, Art. no. eabd5175.

[40] C. Horváth, L. F. Tóth, I. Ulbert, and R. Fiáth, "Dataset of cortical activity recorded with high spatial resolution from anesthetized rats," *Sci. Data*, vol. 8, no. 1, p. 180, Jul. 2021.

[41] P. T. Kuokkanen et al., "Contribution of action potentials to the extracellular field potential in the nucleus laminaris of barn owl," *J. Neurophysiol.*, vol. 119, no. 4, pp. 1422–1436, Apr. 2018.

[42] E. Guzman, Z. Cheng, P. K. Hansma, K. R. Tovar, L. R. Petzold, and K. S. Kosik, "Extracellular detection of neuronal coupling," *Sci. Rep.*, vol. 11, no. 1, Jul. 2021, Art. no. 14733.

[43] J. Lim et al., "Hybrid graphene electrode for the diagnosis and treatment of epilepsy in free-moving animal models," *NPG Asia Mater.*, vol. 15, no. 1, pp. 1–12, Feb. 2023.

[44] B. Ghane-Motlagh and M. Sawan, "Design and implementation challenges of microelectrode arrays: A review," *Mater. Sci. Appl.*, vol. 4, no. 8, pp. 483–495, 2013.

[45] L. Merken, M. Schelles, F. Ceyssens, M. Kraft, and P. Janssen, "Thin flexible arrays for long-term multi-electrode recordings in macaque primary visual cortex," *J. Neural Eng.*, vol. 19, no. 6, Dec. 2022, Art. no. 066039.

[46] Y. Fang et al., "Polarization beam splitter based on Si_3N_4/SiO_2 horizontal slot waveguides for on-chip high-power applications," *Sensors*, vol. 20, no. 10, p. 2862, May 2020.

[47] R. Soref and B. Bennett, "Electrooptical effects in silicon," *IEEE J. Quantum Electron.*, vol. QE-23, no. 1, pp. 123–129, Jan. 1987.

[48] E.-K. Tien, X.-Z. Sang, F. Qing, Q. Song, and O. Boyraz, "Ultrafast pulse characterization using cross phase modulation in silicon," *Appl. Phys. Lett.*, vol. 95, no. 5, Aug. 2009, Art. no. 051101.

[49] O. Boyraz, P. Koonath, V. Raghunathan, and B. Jalali, "All optical switching and continuum generation in silicon waveguides," *Opt. Exp.*, vol. 12, no. 17, p. 4094, 2004.

[50] E.-K. Tien et al., "Discrete parametric band conversion in silicon for mid-infrared applications," *Opt. Exp.*, vol. 18, no. 21, p. 21981, Oct. 2010.

[51] E. A. Kiyatkin, "Brain temperature and its role in physiology and pathophysiology: Lessons from 20 years of thermorecording," *Temperature*, vol. 6, no. 4, pp. 271–333, Oct. 2019, doi: 10.1080/23328940.2019.1691896.